Theoretical Interpretation of Impulse Response Tests of Embedded Concrete Structures

Niels Saabye Ottosen[1]; Matti Ristinmaa[2]; and Allen G. Davis[3]

Abstract: For a concrete beam resting on a bed of sand, an analytical solution technique is derived by which the mobility can be identified. To achieve realistic predictions, significant damping in the bed needs to be introduced. The modest damping of the concrete has little effect on the mobility for small frequencies whereas it has a significant effect for higher frequencies. An imperfection in the bed in terms of a void increases the mobility dramatically for low frequencies whereas the mobility for higher frequencies is almost unchanged. An imperfection in the beam in terms of honeycombing of the concrete, on the other hand, manifests itself by increasing the mobility for high frequencies while leaving the mobility for small frequencies less influenced. These latter conclusions are in good agreement with field experience for concrete slabs resting on soil.

DOI: 10.1061/(ASCE)0733-9399(2004)130:9(1062)

CE Database subject headings: Beams; Concrete structures; Foundations; Fourier transform; Impulsive loads; In situ tests; Plates; Viscoelasticity.

Introduction

The impulse response test method is a nondestructive, stress wave test, used to evaluate structural components and elements. Its application to concrete structures is less well known than its application to mechanical structures, and the method has received far less publicity than the recently developed impact-echo test (Sansalone and Street 1997). Both methods are described in the American Concrete Institute (ACI) report (1998).

Experimental determination of various forms of the frequency response function has been applied for many years in order to characterize the structural response of a diversity of constructions and a comprehensive review is given by Ewins (1984). The method was first adopted in the aviation industry as reported by Kennedy and Pancu (1947); harmonic loadings with different angular frequencies are applied at different locations, and measurement of the response enables one to identify the eigenfrequencies and the eigenmodes. This method is often called the forced vibration method. With $\dot{w}_{\max}$ being the maximum velocity at a point and $f_{\max}$ the maximum load, the mobility is defined as

$$\frac{\dot{w}_{\max}}{f_{\max}} = \text{mobility} \tag{1}$$

where the mobility evidently is a function of the angular frequency of the loading. Mobility is the inverse of impedance, and the acoustic impedance method is used widely in the aeronautical industry in the testing and inspection of aerospace components (Jones and Stiede 1997).

Later, it was realized that it is much easier and more versatile to measure the mobility by striking the element to be tested by a hammer and then make a Fourier transform of the load and of the velocity; this method was earlier named the transient dynamic response or sonic mobility method whereas today it is termed the impulse response method.

The experimental determination of mobility curves for concrete structures occurred at a much later date and focused on the identification of possible faults and defects. In order to evaluate the integrity of concrete drilled piles, the forced vibration method was developed in France in the 1960's and the corresponding theory was reported by Paquet (1968) and Davis and Dunn (1974). Since then, the range of application of the impulse response method to different structural elements has increased to incorporate the following issues: Voiding beneath concrete slabs (Davis and Hertlein 1987), delamination (Davis and Hertlein 1995), honeycombing and cracking (Davis and Hertlein 1995; Davis et al. 1997), evaluation of alkali-silica reaction in concrete piles Davis and Kennedy 1998, and debonding (Davis et al. 1996).

While there has been considerable development of theory to support the results obtained from testing deep foundations (Paquet 1968; Davis and Dunn 1974), no such theory has been developed for testing slab-shaped structural elements. This paper explores the mathematical justification for impulse response test results from concrete slabs supported on a soil subgrade, for the cases where: (1) The slab and soil are in good condition; (2) a void exists in the soil immediately below a portion of the slab; and (3) part of the concrete slab is poorly consolidated.

Test Technique and Typical Results

The impulse response method uses a low-strain impact to send stress waves through the tested element. The impactor is usually a

[1]Professor, Division of Solid Mechanics, Univ. of Lund, Box 118, S-221 00 Lund, Sweden. E-mail: niels_saabye.ottosen@solid.lth.se

[2]Professor, Division of Solid Mechanics, Univ. of Lund, Box 118, S-221 00 Lund, Sweden. E-mail: matti.ristinmaa@solid.lth.se

[3]Senior Principal Engineer, Construction Technology Laboratories, Inc., 5420 Old Orchard Rd., Skokie, IL 60077. E-mail: adavis@ctlgroup.com

Note. Associate Editor: Roger G. Ghanem. Discussion open until February 1, 2005. Separate discussions must be submitted for individual papers. To extend the closing date by one month, a written request must be filed with the ASCE Managing Editor. The manuscript for this paper was submitted for review and possible publication on January 24, 2003; approved on March 16, 2004. This paper is part of the *Journal of Engineering Mechanics*, Vol. 130, No. 9, September 1, 2004. ©ASCE, ISSN 0733-9399/2004/9-1062–1071/$18.00.

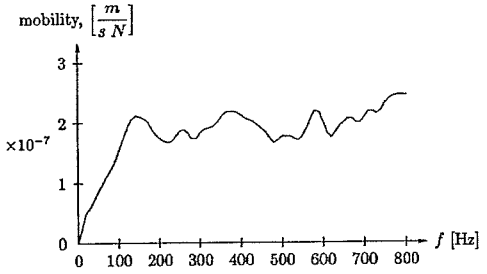

Fig. 1. Typical mobility plot for a sound concrete slab

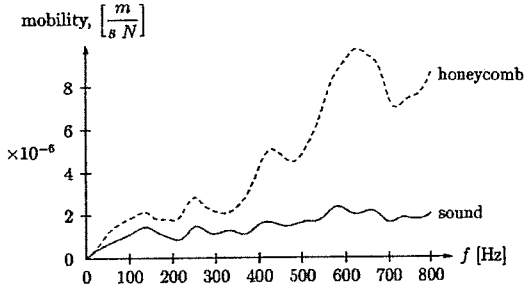

Fig. 2. Typical mobility plots for sound and honeycomb concrete

1-kg sledgehammer with a built-in load cell in the hammerhead. The maximum compressive stress at the impact point in concrete is directly related to the elastic properties of the hammer tip. Typical peak stress levels range from 5 MPa for hard rubber tips to more than 50 MPa for aluminum tips. Response to the input stress is normally measured using a velocity transducer (geophone) placed adjacent to the impact point (direct mobility). This receiver is preferred because of its stability at low frequencies and its robust performance in practice. Both the hammer and the geophone are linked to a portable field computer for data acquisition and storage.

When testing platelike structures, the impact-echo method (Sansalone and Street 1997) uses the reflected stress wave from the base of the concrete element or from some anomaly within that element (requiring a frequency range normally between 3 and 40 kHz). The impulse response test impact, on the other hand, generates a compressive stress approximately 100 times that of the impact-echo test. This greater stress input means that the plate responds to the impulse response hammer impact in a bending mode over a very much lower frequency range (0–800 Hz for plate structures), as opposed to the reflective mode of the impact-echo test.

Both the time records for the hammer force and the geophone velocity response are processed in the field computer using the fast Fourier transform algorithm. The Fourier transform $\dot{W}$ of the velocity and the Fourier transform F of the load are determined; finally, the absolute values $|\dot{W}|$ and $|F|$ of the complex quantities $\dot{W}$ and F are determined and the mobility is then obtained by the relation

$$\frac{|\dot{W}|}{|F|} = \text{mobility} \tag{2}$$

We shall later return to the equivalence between Eqs. (1) and (2). The mobility curve plotted over the range 0 to 800 Hz—a typical example is shown in Fig. 1—contains information on the condition and the integrity of the concrete in the tested element as well as of its soil subgrade. The following observations are used in this evaluation:

- It can be shown mathematically that the initial slope of the mobility curve defines the static compliance, i.e., the static flexibility at the test point in question (static flexibility means that if the structure is loaded statically by a unit force, then the deflection becomes equal to the static flexibility); in practice, this slope is defined as the secant between 0 and 50 Hz.
- Field experience shows that the mean mobility value over the 100–800 Hz range is related to the density and the thickness (i.e., stiffness) of the plate element. A reduction in plate thickness corresponds to an increase in mean mobility. As an example, when total debonding of an upper layer is present, the mean mobility reflects the thickness of the upper debonded layer (in other words, the slab becomes more mobile). Also, any cracking or honeycombing in the concrete will increase the mobility over the tested frequency range. Typical plots illustrating these observations are shown in Fig. 2.
- Field experience shows that when there is loss of support beneath a concrete slab on grade, the initial slope of the mobility curve increases greatly. The peak mobility below 100 Hz becomes appreciable higher than the mean mobility from 100–800 Hz. The ratio of this peak to mean mobility is used as an indicator of the presence and degree of either debonding within the element or voiding/loss of support beneath a slab on grade. Typical plots illustrating these observations are shown in Fig. 3.
- The test results shown in Figs. 1–3 were obtained from reinforced concrete slabs and walls of thickness between 250 and 300 mm, and joint spacing between 2.7 and 5.4 m. The hammer peak forces varied between 4 and 7 MPa, and all velocity responses were recorded using geophones.

In the following, we shall provide a theoretical investigation of these issues.

Fundamental Equations

Our main interest is the behavior of concrete slabs supported by a bed of sand. However, in order to simplify this rather complex problem to one that is amenable to an analytical solution technique, we consider instead a beam supported by a bed of sand; quantitatively, these two problems will differ, but qualitatively they will exhibit similar features. Slab responses are conditioned by the position of the test point on the slab or wall. Tests results toward the slab edges and corners evidently exhibit a higher mobility and lower stiffness than those toward the slab centers. Test results on wall panels often show a lower mobility and higher

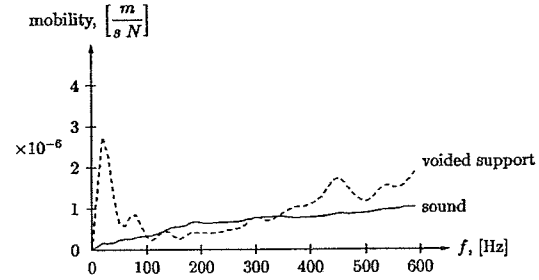

Fig. 3. Typical mobility plots for sound and voided slab support

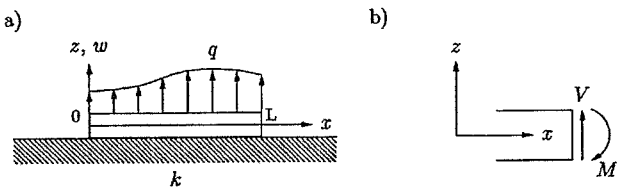

Fig. 4. (a) Problem considered and (b) transverse shear force V and bending moment M

stiffness close to the panel supports, such as columns or floors, because of greater support at those points.

The problem at hand is then shown in Fig. 4(a), where q is the external load per unit length (N/m), k is the bed modulus with dimension (N/m^2), and w is the deflection. Positive directions for the transverse shear force V and the bending moment M are shown in Fig. 4(b) and we have

$$V=\int_A \sigma_{xz}dA, \quad M=\int_A \sigma_{xx}z dA \tag{3}$$

where A = cross-sectional area of the beam.

The mass density of the beam is denoted by ρ and the beam mass per unit length m is therefore $m=\rho A$. Assuming the bed to be viscous in the form of a Kelvin material, the equation of motion in the vertical direction then becomes

$$\frac{\partial V}{\partial x}=-q+kw+c_b\dot{w}+m\ddot{w} \tag{4}$$

where c_b = viscous damping coefficient of the bed with the dimension (Pa s); moreover, a dot denotes the time derivative. Ignoring rotational inertia forces, moment equilibrium requires

$$\frac{\partial M}{\partial x}=V \tag{5}$$

The combination of Eqs. (4) and (5) results in

$$\frac{\partial^2 M}{\partial x^2}=-q+kw+c_b\dot{w}+m\ddot{w} \tag{6}$$

The beam is assumed to be of the Bernoulli type and choosing the x axis to be located at the centroid of the cross section, we have

$$\epsilon_{xx}=-zw'' \tag{7}$$

where $w''=\partial^2 w/\partial x^2$. Assuming also the beam material to be viscous in the form of the Kelvin model, the constitutive equation is given by

$$\sigma_{xx}=E\epsilon_{xx}+\eta\dot{\epsilon}_{xx} \tag{8}$$

where E = Young's modulus and η = viscosity parameter with the dimension (Pa s). The combination of Eqs. (7) and (8) gives

$$\sigma_{xx}=-Ezw''-\eta z\dot{w}'' \tag{9}$$

The insertion of Eq. (9) in the equation on the right in Eq. (3), then provides

$$M=-EIw''-\eta I\dot{w}'' \tag{10}$$

where $I=\int_A z^2 dA$ = moment of inertia. Finally, the use of Eq. (10) in Eq. (6) provides the differential equation sought

$$EIw''''+\eta I\dot{w}''''+kw+c_b\dot{w}+m\ddot{w}=q \tag{11}$$

This equation holds for any part of the beam in which E, I, η, k, c_b, and m are constants.

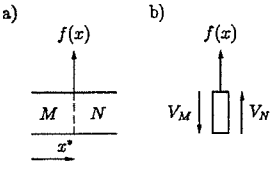

Fig. 5. Beam part immediately left and right of position x^* is called M and N, respectively

Fourier Transform

In Eq. (11), the deflection w is a function of position x and time t, i.e., $w=w(x,t)$. However, instead of time t and in accordance with the test procedure, it turns out to be convenient to work in the frequency domain ω. For this purpose, the Fourier transform $W(x,\omega)$ of the function $w(x,t)$ is defined by

$$W(x,\omega)=\int_{-\infty}^{\infty} w(x,t)e^{-i\omega t}dt \tag{12}$$

where i = imaginary unit, i.e., $i=\sqrt{-1}$. In analogy with Eq. (12), the Fourier transform $\dot{W}$ of $\dot{w}$ is defined by

$$\dot{W}(x,\omega)=\int_{-\infty}^{\infty} \dot{w}(x,t)e^{-i\omega t}dt$$

and, cf. for instance Wolf (1951), it appears that

$$\dot{W}(x,\omega)=i\omega W(x,\omega), \text{ i.e., } \ddot{W}(x,\omega)=-\omega^2 W(x,\omega) \tag{13}$$

In the case considered, the external loading is a point force located at point x^*, i.e.,

$$q(x,\omega)=\delta(x-x^*)f(t) \tag{14}$$

where $\delta(x-x^*)$ denotes Dirac's delta function. In the present case, $\delta(x-x^*)$ therefore has the dimension (1/m) and the strength $f(t)$ of the point force has the dimension of (N). In analogy with Eq. (12), we obtain

$$Q(x,\omega)=\int_{-\infty}^{\infty} q(x,t)e^{-i\omega t}dt, \text{ i.e., } Q(x,\omega)=\delta(x-x^*)F(\omega) \tag{15}$$

where

$$F(\omega)=\int_{-\infty}^{\infty} f(t)e^{-i\omega t}dt \tag{16}$$

With these results and taking the Fourier transform of both sides of Eq. (11), it follows that

$$(EI+i\eta I\omega)W''''-(m\omega^2-k-i\omega c_b)W=\delta(x-x^*)F(\omega) \tag{17}$$

Boundary Conditions

The beam is assumed to be supported by the bed only. Therefore, $M=V=0$ holds at $x=0$ and $x=L$. With Eqs. (10) and (5) and taking the Fourier transform, it follows that

$$W''(0,\omega)=0; \quad W'''(0,\omega)=0$$
$$W''(L,\omega)=0; \quad W'''(L,\omega)=0 \tag{18}$$

The point force $f(t)$ acts at position x^*. The part of the beam immediately to the left- and right-hand side of this point is called M and N, respectively, as shown in Fig. 5(a). From Fig. 5(b), we

have

$$f(t)=V_M-V_N$$

The insertion of Eqs. (5) and (10) and taking the Fourier transform, we obtain

$$\frac{F(\omega)}{EI+i\eta I\omega}=-W_M'''+W_N''' \tag{19}$$

Evidently, the displacement w, the slope w' and the bending moment M are the same immediately to the left- and right-hand side of point x^*. Taking the Fourier transform, it follows that

$$W_M=W_N;\quad W_M'=W_N';\quad W_M''=W_N'' \tag{20}$$

If E, I, η, k, c_b, and m = constants throughout $0\leq x\leq L$, then the position x^* divides the beam into two regions (M and N) and in each region we have, from Eq. (17), that

$$W''''-\frac{m\omega^2-k-i\omega c_b}{EI+i\eta I\omega}W=0 \tag{21}$$

Integration of this fourth-order differential equation provides four arbitrary constants. For the entire beam, eight arbitrary constants emerge and these constants are determined by the eight conditions provided by Eqs. (18)–(20).

Integration of Fourth-Order Differential Equation (21)

The differential equation (21) can be written as

$$W''''-\Lambda W=0 \tag{22}$$

where the complex quantity Λ is given by

$$\Lambda=a+ib \tag{23}$$

and where the real numbers a and b are defined by

$$a=\frac{(m\omega^2-k)EI-c_b\eta I\omega^2}{(EI)^2+(\eta I)^2\omega^2};\quad b=-\frac{(m\omega^2-k)\eta I+c_bEI}{(EI)^2+(\eta I)^2\omega^2}\omega \tag{24}$$

It appears that if damping effects are ignored, i.e., $c_b=\eta=0$, then $a=(m\omega^2-k)/EI$, $b=0$, i.e., Λ becomes a real number.

A solution to the homogeneous differential equation (22) is evidently of the form

$$W=Ce^{\lambda x} \tag{25}$$

where C and λ = constants. Insertion into Eq. (22) provides

$$\lambda^4=\Lambda=a+ib \tag{26}$$

Define the following quantities

$$p=\sqrt{\frac{\sqrt{a^2+b^2}+a}{2}};\quad q=\sqrt{\frac{\sqrt{a^2+b^2}-a}{2}}$$

$$r=\sqrt{\frac{\sqrt{p^2+q^2}+p}{2}};\quad s=\sqrt{\frac{\sqrt{p^2+q^2}-p}{2}} \tag{27}$$

then the solution to Eq. (26) becomes:

- If $b\geq 0$, then

$$\lambda_1=r+is;\quad \lambda_2=-r-is;\quad \lambda_3=s-ir;\quad \lambda_4=-s+ir \tag{28}$$

- If $b\leq 0$, then

$$\lambda_1=r-is;\quad \lambda_2=-r+is;\quad \lambda_3=s+ir;\quad \lambda_4=-s-ir \tag{29}$$

The solution to the homogeneous differential equation (22) then becomes

$$W(x,\omega)=C_1K_1(x,\omega)+C_2K_2(x,\omega)+C_3K_3(x,\omega)+C_4K_4(x,\omega) \tag{30}$$

where C_1, C_2, C_3 and C_4 = arbitrary constants and the functions K_1, K_2, K_3, and K_4 are given by

$$K_1(x,\omega)=e^{\lambda_1 x};\quad K_2(x,\omega)=e^{\lambda_2 x};\quad K_3(x,\omega)=e^{\lambda_3 x}$$

$$K_4(x,\omega)=e^{\lambda_4 x} \tag{31}$$

Perfect Beam Supported by Perfect Bed

The situation is shown in Fig. 6. Let the arbitrary constants C_1, C_2, C_3, and C_4 refer to region M of the beam whereas the arbitrary constants C_5, C_6, C_7, and C_8 refer to region N of the beam. Using Eq. (30), as well as the boundary conditions (18)–(20), we get the following equation system

$$\begin{bmatrix} K_1''(0) & K_2''(0) & K_3''(0) & K_4''(0) & 0 & 0 & 0 & 0 \\ K_1'''(0) & K_2'''(0) & K_3^{IK}(0) & K_4^{IK}(0) & 0 & 0 & 0 & 0 \\ 0 & 0 & 0 & 0 & K_1''(L) & K_2''(L) & K_3''(L) & K_4''(L) \\ 0 & 0 & 0 & 0 & K_1'''(L) & K_2'''(L) & K_3'''(L) & K_4'''(L) \\ -K_1'''(x^*) & -K_2'''(x^*) & -K_3'''(x^*) & -K_4'''(x^*) & K_1'''(x^*) & K_2'''(x^*) & K_3'''(x^*) & K_4'''(x^*) \\ K_1(x^*) & K_2(x^*) & K_3(x^*) & K_4(x^*) & -K_1(x^*) & -K_2(x^*) & -K_3(x^*) & -K_4(x^*) \\ K_1'(x^*) & K_2'(x^*) & K_3'(x^*) & K_4'(x^*) & -K_1'(x^*) & -K_2'(x^*) & -K_3'(x^*) & -K_4'(x^*) \\ K_1''(x^*) & K_2''(x^*) & K_3''(x^*) & K_4''(x^*) & -K_1''(x^*) & -K_2''(x^*) & -K_3''(x^*) & -K_4''(x^*) \end{bmatrix} \begin{bmatrix} C_1 \\ C_2 \\ C_3 \\ C_4 \\ C_5 \\ C_6 \\ C_7 \\ C_8 \end{bmatrix} = \begin{bmatrix} 0 \\ 0 \\ 0 \\ 0 \\ \dfrac{F(\omega)}{EI+i\eta I\omega} \\ 0 \\ 0 \\ 0 \end{bmatrix} \tag{32}$$

where the dependence of K_i on the angular frequency ω is not explicitly shown. In matrix format, this equation system can be written as

$$\mathbf{AC}=\mathbf{f} \tag{33}$$

where $\mathbf{A}=8\times 8$ coefficient matrix; $\mathbf{C}$ contains the parameters

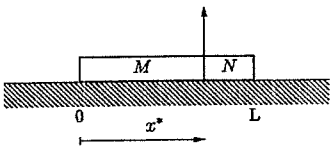

Fig. 6. Perfect beam supported by perfect bed; the point force is located at position x^*

$C_1, C_2, \ldots, C_8$; and $\mathbf{f}$=right-hand side of Eq. (32). It follows immediately that $\det \mathbf{A}=0$ provides the (complex) eigenfrequencies of the system. When $\det \mathbf{A}\neq 0$, we obtain from Eq. (33)

$$\mathbf{C}=\mathbf{A}^{-1}\mathbf{f}, \text{ i.e., } C_i=\sum_{j=1}^{8} A_{ij}^{-1} f_j$$

Except for f_5, all f_j-components are zero, i.e., we obtain

$$C_i=A_{i5}^{-1} f_5 \quad \text{where} \quad f_5=\frac{F(\omega)}{EI+i\eta I\omega} \tag{34}$$

At the position of the point force, i.e., $x=x^*$, we have

$$W(x^*,\omega)=C_1K_1(x^*,\omega)+C_2K_2(x^*,\omega)+C_3K_3(x^*,\omega)+C_4K_4(x^*,\omega)$$

which with Eq. (34) takes the format

$$W(x^*,\omega)=H(\omega)F(\omega) \tag{35}$$

where

$$H(\omega)=\frac{1}{EI+i\eta I\omega}\sum_{i=1}^{4} A_{i5}^{-1}K_i(x^*,\omega) \tag{36}$$

is the complex frequency response function.

In accordance with the test procedure described previously, here we have derived the complex frequency response function taking the Fourier transform of the relevant equations. However, from a physical point of view and in order to enhance later interpretations, a somewhat different approach shall now be adopted.

Assume that the point force varies harmonically with the angular frequency ω, i.e.,

$$f(t)=f_0e^{i\omega t}. \tag{37}$$

where f_0=constant real quantity and where it is implicitly understood that, say, $f(t)=\mathrm{Im}(f_0e^{i\omega t})=f_0\,\mathrm{Im}(e^{i\omega t})$; f_0 is therefore the force amplitude. The steady-state response then also varies harmonically with the phase angle ϕ, i.e.,

$$w(x,t)=w_0(x)e^{i(\omega t+\phi)} \text{ or } w(x,t)=\hat{w}_0(x)e^{i\omega t}$$
$$\text{where } \hat{w}_0(x)=w_0(x)e^{i\phi} \tag{38}$$

where $w_0(x)$=real quantity, namely the deflection amplitude.

It appears from Eq. (38) that $\dot{w}=i\omega w$ and $\ddot{w}=-\omega^2 w$ and the similarity with the properties of the Fourier transform is evident, cf. Eq. (13). The insertion of Eqs. (37) and (38) into Eqs. (11) and (14) then reveals that, with W replaced by $\hat{w}_0$ and F replaced by f_0, all derivations will be similar to the previous ones and the result immediately becomes

$$\hat{w}_0(x^*)=H(\omega)f_0 \tag{39}$$

In fact, this approach to determination of the complex frequency response function finds its analogue in the forced vibration method where harmonic loadings are applied at different frequencies and the response is measured, as discussed previously. It follows from Eq. (39) that

$$|\hat{w}_0(x^*)|=|w_0(x^*)|=|H(\omega)||f_0| \Rightarrow \frac{w_0(x^*)}{f_0}=|H(\omega)| \tag{40}$$

where $|H(\omega)|$ denotes the absolute value of the complex quantity $H(\omega)$. Therefore, the absolute value of the complex frequency response function provides the relation between the amplitude of deflection and amplitude of force; i.e. $|H(\omega)|$ is the dynamic flexibility, i.e., the dynamic compliance, at the point in question. For very small frequencies, inertia forces are of no importance, i.e.,

$$|H(\omega=0)|=\text{static compliance} \tag{41}$$

With these remarks, we return to the Fourier transform technique. From Eqs. (13) and (35), it follows that

$$\dot{W}(x^*,\omega)=Y(\omega)F(\omega) \text{ where } Y(\omega)=i\omega H(\omega) \tag{42}$$

where $Y(\omega)$=complex mobility. In accordance with Eq. (2), we then get

$$\frac{|\dot{W}(x^*,\omega)|}{|F(\omega)|}=|Y(\omega)|=\text{mobility} \tag{43}$$

and from the equation on the right-hand side of Eq. (42), we have

$$|Y(\omega)|=\omega|H(\omega)|, \text{ i.e., } \frac{d|Y(\omega)|}{d\omega}=|H(\omega)|+\omega\frac{d|H(\omega)|}{d\omega}$$

i.e.,

$$\left(\frac{d|Y(\omega)|}{d\omega}\right)_{\omega\to 0}=|H(\omega=0)|=\text{static compliance} \tag{44}$$

as already mentioned in relation to the test results.

Results from the analysis presented above shall now be shown and discussed; choosing a fixed value of the frequency ω all calculations were performed. By ignoring damping effects in the first place, the following data were adopted:

$$\text{beam height}=0.2 \text{ m, beam width}=0.1 \text{ m,}$$
$$\text{beam length}=4 \text{ m}$$
$$\rho=2{,}300 \text{ kg/m}^3, \quad E=2.5\times 10^{10} \text{ Pa}, \quad k=10^7 \text{ Pa} \tag{45}$$

The mass density and Young's modulus are typical for concrete. So-called rigid-body motion refers to the free vibration mode in which the beam vibrates as a rigid body on the foundation, cf. the discussion in Appendix A. It is shown there that the eigenfrequency of the first bending mode is always above the rigid-body eigenfrequency. With the data of Eq. (45) and the results in Appendix A, we obtain $f_{rb}=74.2$ Hz (rigid-body motion) and $f_{bm}=85.4$ Hz (first bending mode), i.e., $f_{bm}/f_{rb}=1.15$. These frequencies are typical for the ones found in field experience. Moreover, the frequency range up until 1,000 Hz ($f=\omega/2\pi$) is typically considered in praxis.

With these data, the mobility curve for the undamped structure takes the form shown in Fig. 7. The eigenfrequencies are clearly visible and from Appendix A, the rigid-body eigenfrequency becomes $f_{rb}=74.2$ Hz whereas the eigenfrequencies for the first seven bending modes become $f_{bm}=85.4$, 138, 241, 386, 570, 793, and 1054 Hz; evidently, these eigenfrequencies correspond exactly to the ones appearing in Fig. 7.

To determine the eigenmodes corresponding to free vibrations, equation system (33) reduces to $\mathbf{AC}=\mathbf{0}$. Each eigenfrequency results in $\det \mathbf{A}=0$ and the corresponding $\mathbf{C}$ vector is then determined and used to identify the corresponding eigenmode. In this fashion, the rigid-body motion and the first seven bending modes

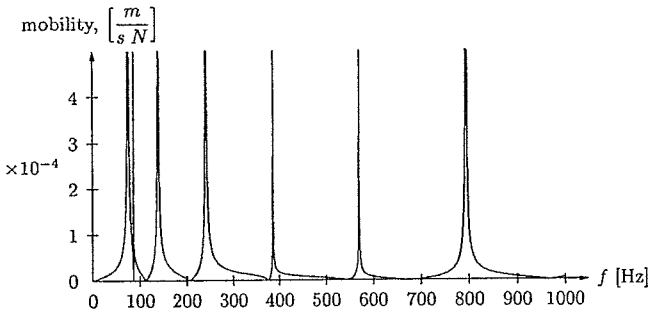

Fig. 7. Mobility curve for undamped conditions; impulse applied at $x=3$ m

for undamped conditions are shown in Fig. 8. The effect that the beam is not loaded by either bending moments or transverse shear forces at its ends is clearly visible.

Another point of interest is that the mobility curve shown in Fig. 4 for the undamped structure has an appearance that is far from those found in the field, cf. Fig. 1. The only possible explanation is that damping must be included in the analysis and that damping effects are expected to be significant.

In the first place, we only consider damping in the bed whereas the concrete material is undamped. The results are shown in Fig. 9 where, for instance, $c_b=1{,}200$ Pa corresponds to the damping ratio $\xi=2.8\%$ for the rigid-body motion, cf. Appendix A. Due to the damping of the bed, Fig. 9 shows that bending eigenmodes also become damped and this is in accordance with the results given in Appendices A and B.

Since the loading consists of a point force, we can never excite a pure rigid-body motion even when the frequency equals the rigid-body eigenfrequency. At that frequency, the response is dominated by the rigid-body motion with small contributions from the first bending mode. Moreover, Fig. 7 shows that the first bending eigenfrequency is very close to the rigid-body eigenfrequency and Fig. 8 reveals that the point force acts at a position

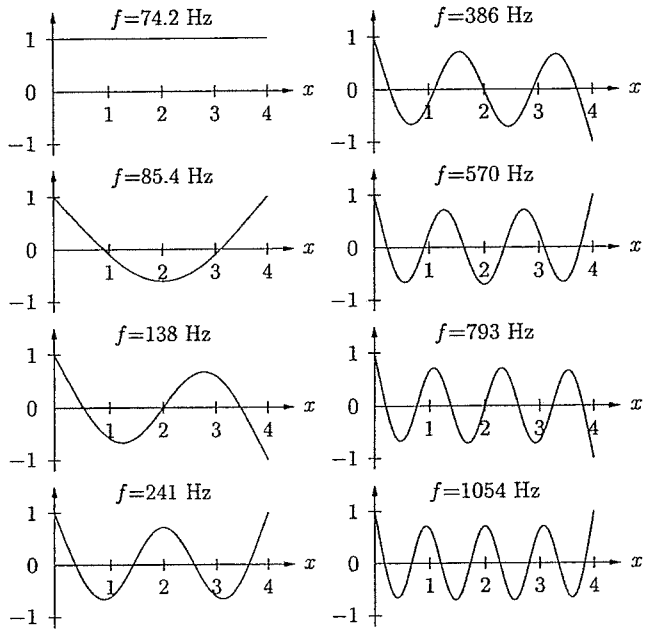

Fig. 8. Rigid-body motion and the first seven bending modes for undamped conditions.

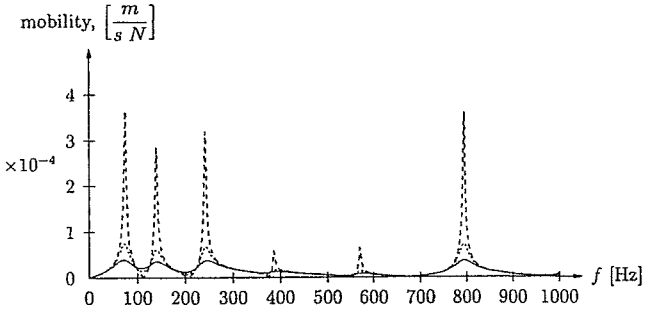

Fig. 9. Mobility curves considering damping of the bed for $c_b=1{,}200$ Pa s ($\xi=2.8\%$, dashed line), 6,000 Pa s ($\xi=14\%$, dotted line), and 12,000 Pa s ($\xi=28\%$, full line). No damping in the concrete; impulse applied at $x=3$ m.

($x=3$ m) close to a node of the first bending mode. Therefore, the first maximum of any of the mobility curves shown in Fig. 9 is due to a combination of the rigid-body motion and the first bending mode and the eigenfrequencies for the rigid-body motion and the first bending mode cannot be identified from the curves; however, for the higher bending modes, the corresponding eigenfrequencies are clearly visible from Fig. 9.

Comparing Fig. 9 with typical mobility curves obtained in the field, it is concluded that significant damping in the bed must be present. This observation is in accordance with the data used by Chng (1992) in his analysis of concrete slabs on sand. Using the finite element method, Chng ignored damping in the concrete slab and adopted a damping ratio for the bed that corresponds approximately to $\xi\approx 20\%$.

With this discussion, we shall in the subsequent calculations adopt the following damping property of the bed

$$c_b=12{,}000 \text{ Pa s, i.e., } \xi=28\% \tag{46}$$

In order to adopt realistic damping properties of the concrete, it is recalled that even when concrete viscosity is ignored, i.e., $\eta=0$, damping of the bed also gives rise to damping of the bending modes, cf. Fig. 9 and Table 2 in Appendix B. Based on Table 2, a realistic concrete viscosity must be below, say, $\eta=1.88\times 10^6$ Pa s. For $\eta=0$, 4.70×10^5 and 1.88×10^6 Pa s, the corresponding mobility curves are shown in Fig. 10. Based on these curves as well as the considerations in Appendix B, we choose in the subsequent calculations the following damping parameter for the concrete

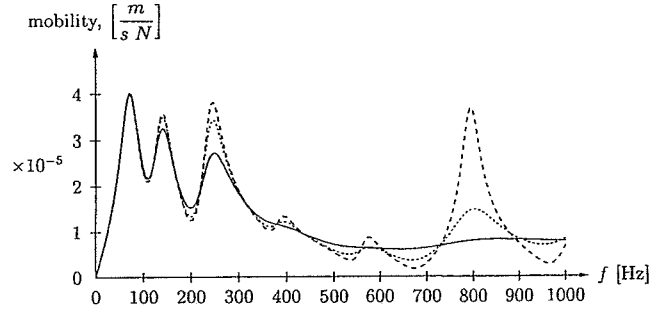

Fig. 10. Mobility curves considering damping of the bed ($c_b=12{,}000$ Pa s) and damping of the concrete for $\eta=0$ (undamped, dashed line), $\eta=4.70\times 10^5$ (dotted line), and $\eta=1.88\times 10^6$ Pa s (full line); impulse applied at $x=3$ m.

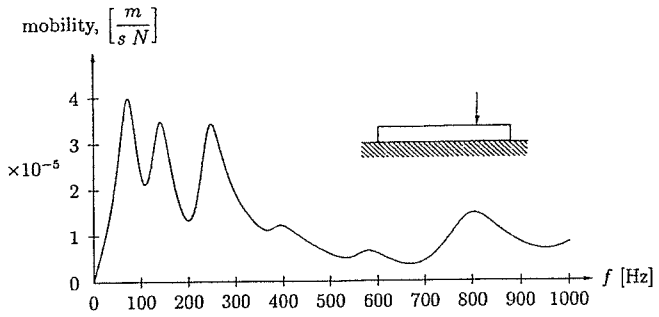

Fig. 11. Mobility curve for perfect beam resting on a perfect bed, $\eta = 4.70 \times 10^5$ Pa s (concrete) and $c_b = 12{,}000$ Pa s (bed); impulse applied at $x = 3$ m.

$$\eta = 4.70 \times 10^5 \text{ Pa s} \tag{47}$$

The mobility curve for the perfect beam resting on a perfect bed then takes the form shown in Fig. 11.

It is recalled from Appendix A that in a pure rigid-body motion, the constitutive data of the concrete beam has no influence at all; this is evident since in a pure rigid-body motion, the beam acts as a rigid body. As we load the beam by a point force, a pure rigid-body motion can never be excited, but close to the rigid-body eigenfrequency, the response is dominated by the rigid-body motion with only small contributions from the first bending mode. These observations are supported by Fig. 10 where changes of the concrete viscosity parameter η only influence the mobility curves insignificantly for frequencies close to the rigid-body eigenfrequency. However, for higher frequencies, Fig. 10 shows that the concrete viscosity η influences the mobility curves significantly.

As previously discussed, the maximum of the mobility curve is determined primarily by the bed properties. In Fig. 11, the mobility in general decreases significantly after its maximum value around the rigid-body motion and this decrease is not found in typical mobility curves obtained in practice, cf. Figs. 1–3. However, we are considering a beam and a beam only allows bending in one direction whereas a plate allows bending in two directions. All other things equal, a plate is therefore more flexible than the corresponding beam and this explains the difference between Fig. 11 and Figs. 1–3. Here, however, we are especially concerned about the influence of various defects in the structure and how these defects qualitatively influence the mobility curve and the difference discussed above is therefore of minor importance.

Imperfect Beam on Imperfect Bed

With this discussion of the response of a perfect beam resting on a perfect bed, we next investigate the mobility curves when imperfections occur in the beam or in the bed; indeed, the use of the impulse response method is in practice concerned with identification of such imperfections. A vast field experience on this issue has been accumulated over the years, but no systematic theoretical interpretation seems to be present in the literature.

The situation for an imperfect beam on an imperfect bed is illustrated in Fig. 12. The boundary conditions between, say, region 1 and 2 are evidently that the displacement, slope, bending moment, and transverse shear force are identical immediately to the left- and right-hand side of point $x = L_1$. With the boundary conditions at $x = 0$ and $x = L$ given by Eq. (18), the boundary

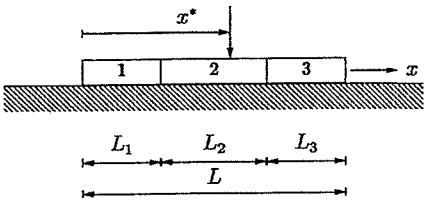

Fig. 12. Imperfect beam and imperfect bed; the beam and bed are divided into three regions each with its own constant material parameters.

conditions where the point force acts, i.e., $x = x^*$, given by Eqs. (19) and (20), we therefore end up with an equation system similar to Eqs. (32) and (33) except that now the coefficient matrix becomes a 16×16 matrix. The solution procedure therefore follows that already described previously for the perfect beam on the perfect bed.

Void in the Bed. Imperfections in the bed often take the form of a void in the bed; in that region, the bed properties are taken as $k = 0$ and $c_b = 0$ and Fig. 13 shows the mobility curves for the sound system and when a void is present ($2.5 \text{ m} \leq x \leq 3.5$ m). Due to the existence of such a void, the eigenmode in terms of a rigid-body motion is lost. In Fig. 14, the first eight undamped eigenmodes are shown. As discussed above, no eigenmode in terms of a pure rigid-body motion exists and all eigenmodes are bending modes. Apart from that, a comparison with Fig. 8 shows that the higher-order bending modes are nearly independent of the bed properties and this is in accordance with the discussion in Appendix A. The mobility curves in Fig. 13 show that the smallest eigenfrequency, which is dominated by the stiffness of the bed, is lowered due to the void since the total stiffness of the bed is lowered.

Since the total stiffness of the bed is lowered, Fig. 13 even shows that the mobility, i.e., also the dynamic flexibility, is increased dramatically for small frequencies when compared with the sound system. On the other hand, Fig. 13 shows that the mobility curve for higher frequencies, i.e., higher-order bending modes, is almost independent of the bed properties and this observation is in accordance with the discussion above.

Honeycombing in the Beam. Imperfections in the beam often take the form of honeycombing of the concrete. In that region, we take as a sample Young's modulus to be one quarter of the perfect concrete, i.e., $E = 2.5 \times 10^{10}/4$ Pa. Also the viscosity η of the con-

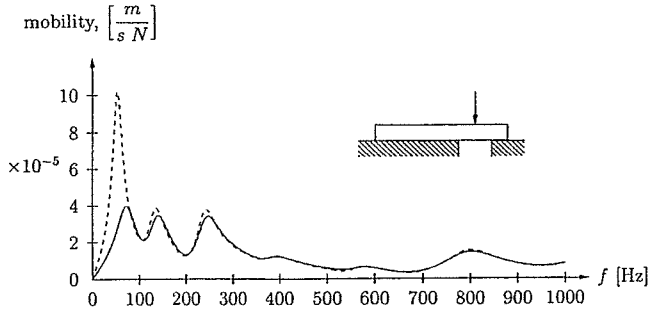

Fig. 13. Mobility curves for sound system (full line) and for a void in the bed (dashed line), the void being located between $2.5 \text{ m} \leq x \leq 3.5$ m; impulse applied at $x = 3$ m.

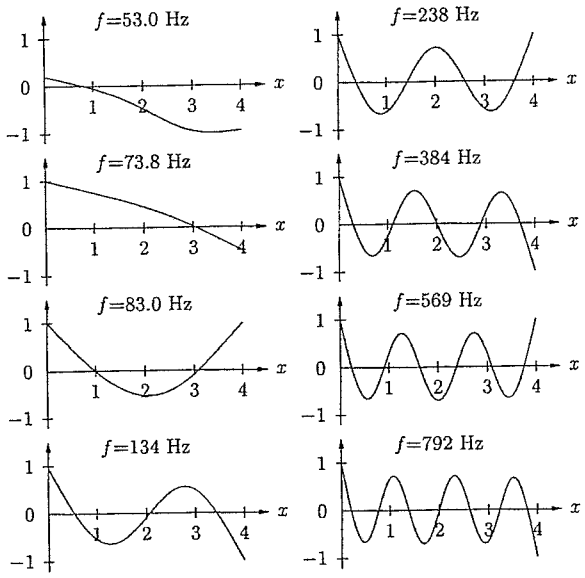

Fig. 14. Void in the bed in the region 2.5 m$\leq x \leq$3.5 m. First eight undamped eigenmodes; no rigid-body motion exists

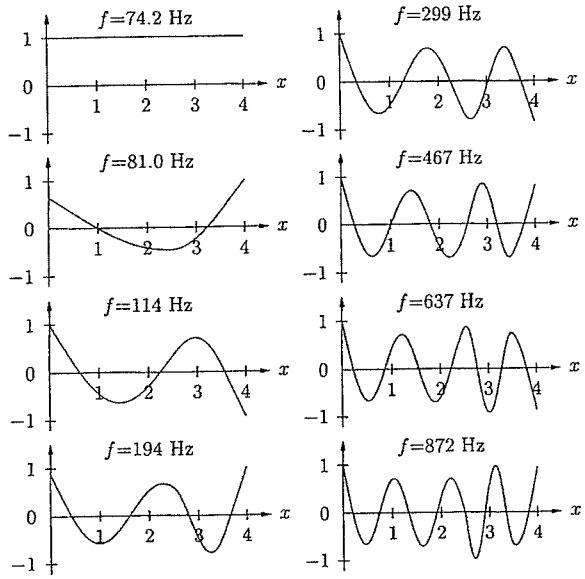

Fig. 16. Honeycombing of the beam ($E=2.5\times10^{10}/4$ Pa), honeycombing being located between 2.5 m$\leq x \leq$3.5 m. Rigid-body motion and the first seven bending modes for undamped conditions

crete then needs to be modified in the honeycomb region. As we are considering concrete material parameters, we ignore for the moment the bed support and assume that the entire beam consists of honeycomb concrete. From Eq. (52), it then follows that $\xi = \beta^4 \eta I/(2m\omega_0)$. It appears readily from this expression—as well as from Table 1 in Appendix B—that $\eta=4.70\times10^5$ Pa s, cf. Eq. (47), corresponds to $\xi=0.25\%$ relative damping of the first bending mode. Adopting this damping ratio and considering that the E modulus now is $2.5\times10^{10}/4$ Pa, we obtain $\eta=2.35\times10^5$ Pa s. Therefore, in the damaged part of the beam, we have $E=2.5\times10^{10}/4$ Pa and $\eta=2.35\times10^5$ Pa s. In the remaining (sound) part of the beam, the parameters are as before given by $E=2.5\times10^{10}$ Pa and $\eta=4.70\times10^5$ Pa s.

The mobility curves for the sound system and for an imperfection in terms of a region (2.5 m$\leq x \leq$3.5 m) with honeycombing of the concrete are shown in Figs. 15 and 16 shows the first eight undamped eigenmodes. Now the eigenmode in terms of a pure rigid-body motion is recovered whereas the remaining seven eigenmodes are bending modes. A comparison of Figs. 16 and 8 shows that it is mostly the higher-order bending modes that are influenced by honeycombing of the concrete. In that region of the beam, the displacements of the eigenmodes are increased and the distance between the nodes of the bending modes is decreased.

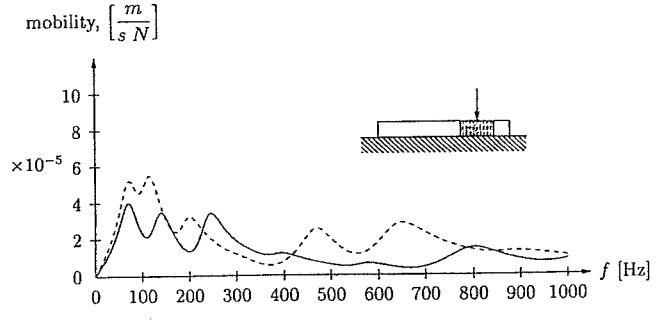

Fig. 15. Mobility curves for sound system (full line) and for honeycombing (dashed line) in the beam ($E=2.5\times10^{10}/4$ Pa), honeycombing being located between 2.5 m$\leq x \leq$3.5 m; impulse applied at $x=3$ m.

Conclusions

The analytical solution technique derived allows for a systematic interpretation of impulse response tests and special emphasis has been given to the qualitative influence of defects in terms of voids in the bed and honeycombing in the concrete. In the modeling process, it has been shown that the effects of damping are very important. Significant damping of the bed needs to be considered, but even much more modest damping in the concrete has an important influence on the mobility curve.

According to the simulations, a void in the bed will increase the mobility dramatically for small frequencies whereas it leaves the mobility curve unchanged for higher frequencies. On the other hand, honeycombing in the concrete will increase the mobility for high frequencies whereas the influence for small frequencies is less significant. These conclusions are in good agreement with field experience for concrete slabs resting on soil.

Appendix I. Free Vibrations with Damping

For a perfect beam on a perfect bed, free vibrations are investigated. Since the external loading $q=0$, Eq. (11) reduces to

$$EIw'''' + \eta I\dot{w}'''' + kw + c_b\dot{w} + m\ddot{w} = 0 \tag{48}$$

Let the displacement be written in the form

$$w(x,t) = f(x)g(t) \tag{49}$$

Insertion into Eq. (48) then provides the following two equations:

$$f'''' - C_1 f = 0 \tag{50}$$

$$\ddot{g} + 2\xi\omega_0\dot{g} + \omega_0^2 g = 0 \tag{51}$$

where C_1 = real constant to be determined from the boundary conditions and the quantities ξ and ω_0 are defined by

Table 1. Bed Excluded

Concrete viscocity	n / f (Hz)	1 42.4	2 117	3 229	4 378	5 565	6 790	7 1,051
$(\eta=4.70\times10^5)$	ξ (%)	0.25	0.69	1.35	2.24	3.34	4.66	6.21
$(\eta=1.88\times10^6)$	ξ (%)	1.00	2.75	5.41	8.94	13.4	18.7	24.8
$(\eta=7.52\times10^6)$	ξ (%)	4.00	11.0	21.6	35.8	53.4	74.6	99.4

Table 2. Bed Included with $c_b=12{,}000$ Pa s

Concrete viscocity	n / f (Hz)	0 74.2	1 85.4	2 138	3 241	4 386	5 570	6 793	7 1,054
$(\eta=0)$	ξ (%)	28.0	24.3	15.0	8.63	5.38	3.64	2.62	1.97
$(\eta=4.70\times10^5)$	ξ (%)	28.0	24.4	15.6	9.91	7.58	6.95	7.26	8.16
$(\eta=1.88\times10^6)$	ξ (%)	28.0	24.8	17.3	13.8	14.2	16.9	21.2	26.7

$$\xi=\frac{c_b+C_1\eta I}{2m\omega_0};\quad \omega_0^2=\frac{k+C_1EI}{m} \tag{52}$$

With $0\leq\xi\leq1$, the solution to Eq. (51) is evidently given by

$$g(t)=A_0e^{-\xi\omega_0 t}\sin(\omega_0\sqrt{1-\xi^2}t+\phi) \tag{53}$$

where A_0 and ϕ = arbitrary constants determined from the initial conditions. It appears that ξ = damping ratio; ω_0 = undamped angular eigenfrequency; and $\omega_0\sqrt{1-\xi^2}$ = damped angular eigenfrequency.

Since no bending moments or transverse shear forces act at the beam ends, the boundary conditions become

$$f''(0)=0;\quad f'''(0)=0;\quad f''(L)=0;\quad f'''(L)=0 \tag{54}$$

A solution to Eq. (50) is evidently of the form

$$f(x)=C_2e^{\lambda x} \tag{55}$$

where C_2 and λ = constants. Insertion into Eq. (50) results in

$$\lambda^4=C_1;\quad \text{i.e.,}\quad \lambda^4=\frac{\omega_0^2m-k}{EI} \tag{56}$$

If $\omega_0^2m-k=0$, i.e., $\lambda^4=C_1=0$ then

$$\omega_0=\sqrt{\frac{k}{m}} \tag{57}$$

Since $C_1=0$ = the solution to Eq. (50) subjected to the boundary condition (54) becomes

$$f=\alpha_1+\alpha_2x \tag{58}$$

i.e., a rigid-body motion. The undamped eigenfrequency is given by Eq. (57) and the damped eigenfrequency by $\omega_0\sqrt{1-\xi^2}$ where ξ is determined by the equation on the left-hand side of Eq. (52). Therefore, a free vibration with this damped eigenfrequency is possible in which the beam is not deformed at all and the entire structure acts as a one degree of freedom system; this vibration mode is referred to as the rigid-body motion. Since the beam is undeformed, its constitutive parameters do not influence the motion.

If $\omega_0^2m-k>0$, i.e., $\lambda^4=C_1>0$ then

$$\lambda_1=\beta;\quad \lambda_2=-\beta;\quad \lambda_3=i\beta;\quad \lambda_4=-i\beta \tag{59}$$

where

$$\beta=\left(\frac{\omega_0^2m-k}{EI}\right)^{1/4},\quad \text{i.e.,}\quad \beta^4=C_1 \tag{60}$$

Since $f(x)$ = real quantity and recalling the relations $e^x=\cosh x+\sinh x$ and $e^{ix}=\cos x+i\sin x$, the solution to Eq. (50) then becomes

$$f(x)=\alpha_1\cosh\beta x+\alpha_2\sinh\beta x+\alpha_3\cos\beta x+\alpha_4\sin\beta x \tag{61}$$

in accordance with Kamke (1943). Fulfillment of the boundary condition (54) requires

$$\cosh\beta L\cos\beta L=1 \tag{62}$$

It appears that $\beta=0$ is a solution, but this situation has already been considered in Eq. (57). The other solutions to the equation above are given, for instance, by Timoshenko et al. (1974), and we have

n	1	2	3	4	5	6	7
βL	4.730	7.853	10.996	14.137	17.279	20.420	23.562

(63)

where the higher modes for $n\geq3$ with close accuracy is given by $\beta L=(n+1/2)\pi$. The modes identified above are the bending modes of the beam. With this identification of the β parameter the undamped eigenfrequency ω_0 is determined by Eq. (60) and the damped eigenfrequency by $\omega_0\sqrt{1-\xi^2}$ where ξ is determined by the equation on the right-hand side of Eq. (52).

In view of Eq. (52) and since $C_1=\beta^4$, it appears that the investigated free vibrations involve both the beam parameters as well as the bed parameters. Moreover, from Eqs. (60) and (57), it follows that the bending eigenfrequencies always are larger than the rigid-body eigenfrequency. It is observed that the influence on ω_0 of the bed (i.e., the parameter k) decreases with increasing β-values, i.e., increasing ω_0 values. Therefore, higher-order modes are only marginally influenced by the bed modulus k.

If $\omega_0^2m-k<0$, i.e., $\lambda^4=C_1<0$ then

$$\lambda_1=\beta(1+i);\quad \lambda_2=-\beta(1+i);\quad \lambda_3=\beta(1-i)$$
$$\lambda_4=-\beta(1-i) \tag{64}$$

where

$$\beta=\left(\frac{k-\omega_0^2m}{4EI}\right)^{1/4},\quad \text{i.e.,}\quad \beta^4=-\frac{C_1}{4} \tag{65}$$

Since $f(x)$ is a real quantity, the solution to Eq. (50) then becomes

$$f(x)=\alpha_1\cosh\beta x\cos\beta x+\alpha_2\sinh\beta x\cos\beta x$$
$$+\alpha_3\cosh\beta x\sin\beta x+\alpha_4\sinh\beta x\sin\beta x \tag{66}$$

in accordance with Kamke (1943). However, fulfilment of the boundary condition (54) requires

$$\sinh^2 \beta x - \sin^2 \beta x = 0$$

Since $\beta \neq 0$, this equation has no solution, i.e., the situation $\omega_0^2 m - k < 0$ will never occur. In conclusion, only $\omega_0^2 m - k \geq 0$ is of relevance and, as already mentioned, this implies that the rigid-body eigenfrequency is the lowest of all eigenfrequencies.

Appendix II. Damping Considerations

The viscosity parameter c_b for the bed and the viscosity parameter η for the beam influence the damping ration ξ according to Eq. (52). The stiffness data are taken in accordance with Eq. (45) and the following results are used in order to motivate the choice of η.

If the bed is completely ignored, the undamped frequency f and damping ration ξ for the first seven bending modes are then shown in Table 1.

Considering the bed and accepting the bed viscosity $c_b = 12{,}000$ Pa s, we obtain (where $n = 0$ corresponds to the rigid-body motion)

Table 1 shows that the higher-order bending modes are much more damped than the low-order bending modes. Table 2 illustrates that even when damping in the concrete is ignored ($\eta = 0$), all bending modes become damped. For $\eta = 1.88 \times 10^6$ Pa s, all bending modes become heavily damped and a reasonable viscosity parameter for the concrete seems to be $\eta = 4.70 \times 10^5$ Pa s. The results are shown in Table 2.

References

American Concrete Institute (ACI). (1998). "Nondestructive test methods for evaluation of concrete in structures." *ACI 228. 2R-98*, Detroit.

Chng, R. (1992). "Characterizing the integrity of concrete roads/pavements using frequency response function methods." PhD thesis, Dept. of Mechanical Engineering, Univ. of Manchester, U.K.

Davis, A. G., and Dunn, C. S. (1974). "From theory to field experience with the nondestructive vibration testing of piles." *Proc. Inst. Civ. Eng. Part 2.* 59, 867–875.

Davis, A. G., and Hertlein, B. H. (1987). "Nondestructive testing of concrete pavement slabs and floors with the transient dynamic response method." *Proc., Int. Conf. Structural Faults and Repair*, Vol. 2, Univ. of Edinburgh, London, 429–433.

Davis, A. G., and Hertlein, B. H. (1995). "Nondestructive tesing of concrete chimneys and other structures." *Proc. SPIE*, 2457, 129–136.

Davis, A. G., Evans, J. G., and Hertlein, B. H. (1997). "Nondestructive evaluation of concrete radioactive waste tanks." *J. Perform. Constr. Facil.*, 11(4), 161–167.

Davis, A. G., Hertlein, B. H., Lim, M., and Michols, K. (1996). "Impact-echo and impulse response stress wave methods: Advantages and limitations for the evaluation of highway pavement concrete overlays." *Proc. SPIE*, 2946, 88–96.

Davis, A. G., and Kennedy, J. (1998). "Impulse response testing to evaluate the degree of alkali-aggregate reaction in concrete drilled-shaft foundations for electricity transmission towers." *Proc. SPIE*, 3398, 178–185.

Ewins, D. J. (1984). *Modal testing: Theory and practice*, Research Studies, Hartfordshire, U.K.

Jones, M. G., and Stiede, P. E. (1997). "Comparison of methods for determining specific acoustic impedance." *J. Acoust. Soc. Am.*, 101, 2694–2704.

Kamke, E. (1943). *Differentialgleichungen. Lösungsmetoden und Lösungen*, Akademisch Verlagsgesellschaft, Becker&Erler Kom.-Ges., Leipzig, Germany.

Kennedy, C. C., and Pancu, C. D. P. (1947). "Use of vectors in vibration measurement and analysis." *J. Aeronaut. Sci.*, 14(11), 603–625.

Paquet, J. (1968). "Etude vibratoire des pieux en béton: réponse harmonique et impulsionelle application au controle." *Ann. Inst. Tech. Bat. Trav. Publics*, 245, 789–803.

Sansalone, M., and Street, W. B. (1997). *Impact-echo: Nondestructive evaluation of concrete and masonry*, Bullbrier, Ithaca, N.Y.

Timoshenko, S., Young, D. H., and Weaver, W., Jr. (1974). *Vibration problems in engineering*, 4th Ed., Wiley, New York.

Wolf, K. B. (1979). *Integral transforms in science and engineering*, Plenum, New York.